Effect of Rib Angle on Capillary Flow in Closed Hierarchical Microchannels

Gaurav Kumar
Graduate School of Engineering, Kyushu Institute of Technology

Nagayama, Gyoko
Department of Mechanical Engineering, Kyushu Institute of Technology

https://doi.org/10.5109/7323344

出版情報：Proceedings of International Exchange and Innovation Conference on Engineering & Sciences (IEICES). 10, pp.747-753, 2024-10-17. International Exchange and Innovation Conference on Engineering & Sciences
バージョン：

Effect of Rib Angle on Capillary Flow in Closed Hierarchical Microchannels

Gaurav Kumar[1], Gyoko Nagayama[2]
[1]Graduate School of Engineering, Kyushu Institute of Technology, Kitakyushu, Fukuoka 804-8550, Japan
[2]Department of Mechanical Engineering, Kyushu Institute of Technology, Kitakyushu, Fukuoka 804-8550, Japan.
Corresponding author email: nagayama.gyoko725@mail.kyutech.jp

Abstract: *Biomimetic-inspired surfaces have the potential to enhance water transport efficiency, as channels with hierarchical micro/nanoscale structures demonstrate improved capillary flow characteristics. The applicability of the classical Lucas-Washburn equation for capillary-driven flow in open rectangular microchannels has been debated, and its validity for hierarchical microchannels remains uncertain. In this study, numerical simulations using Volume-of-fluid-based OpenFOAM were used to examine the effect of rib angle in hierarchical microchannels, focusing on the impact of fabrication errors on capillary performance. The results indicate that if the rib is not perpendicular to the bottom surface/wall of the channel, capillary performance reduces. With the change in the type of rib inclination, the capillary performance also changes. This study underscores the importance of precise fabrication in optimizing the efficiency of hierarchical microchannels.*

Keywords: Capillary-driven flow; Hierarchical Microchannel; OpenFOAM; Numerical Simulation; Rib Angle

1. INTRODUCTION

Capillary-driven flow, also referred to as capillary wicking, is a widely observed phenomenon in nature that occurs across various scales [1]–[4]. Capillary microfluidic devices utilize this phenomenon effectively, eliminating the need for external power to transport fluids. The interaction between capillary geometry, fluid properties, and solid-liquid interfaces is crucial in determining fluid imbibition [5]. The imbibition rate in capillary-driven channels is often used to evaluate system performance, especially in lab-on-a-chip devices, where rapid fluid sample delivery can speed up sample analysis. Additionally, heat pipes require a higher capillary mass flow rate to move the working fluid from the condenser region to the evaporator region. This ensures the evaporator is consistently supplied with fluid to sustain continuous evaporation and heat absorption. Insufficient capillary mass flow can cause the evaporator to dry out, disrupting the heat transfer process and reducing the heat pipe's efficiency.

In microchannel fluid transportation, the capacity to move fluid is determined by critical pressure, which is influenced by various factors. One key factor is the Laplace pressure (ΔP), which depends on the fluid's interfacial tension, the advancing contact angles (θ) between the fluid and surrounding surfaces, and the microchannel dimensions. The contact angles of the fluid on the inner surfaces of microchannels are dictated by the interfacial forces at the solid-liquid-gas three-phase lines. The Young-Laplace equation expresses the relationship between interfacial tension, contact angle, and the radius of curvature of the capillary, as shown in equation (1).

$$\Delta P = \frac{2\sigma cos cos\,\theta}{r} \tag{1}$$

where σ is the surface tension of the fluid and r is the capillary radius. For several years, various cross-sections of the microchannel have been studied as seen in Fig. 1 [6]. Consequently, any alterations to the physicochemical properties of the inner surfaces of the microchannels will directly affect the original interactions between these surfaces and the liquid transport. These changes will significantly impact flow behaviors at the micro/nanoscale. In recent years, there has been various research on introducing microstructures inside the microchannel which are inspired by nature [7]–[12]. Such microstructures help to enhance the flow characteristics thus improving the transport efficiency and optimizing microchannel devices.

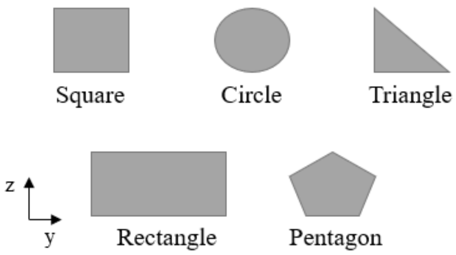

Fig. 1. Different cross-sections of closed microchannel.

Comanns et al. introduced a surface modification inspired by the Texas horned lizard to achieve passive directional liquid transport. By applying the functional geometric principles of 'asymmetry' and 'interconnection', they enhanced the overall fluid transport. Asymmetric capillaries enable directional liquid flow, while interconnections help the liquid overcome obstacles, thus extending the transport distance [13]. In the study conducted by Ju et al., they examined the fog collection abilities of the cactus species *Opuntia microdasys* also known as Bunny ears cactus. The study found that the cactus's survival mechanism includes an efficient fog collection system comprised of clusters of conical spines and trichomes on its stem. Each spine has three integrated parts, each playing distinct roles in fog collection due to its unique surface structures. The efficiency of this system is attributed to the gradient of Laplace pressure, the gradient of surface-free energy, and the integration of multiple functions [14]. Similarly, several studies have been conducted on the surfaces inspired from the hierarchical structure of *Sarracenia trichomes* [15], [16]. Chen et al. investigated water harvesting and transport in the hierarchical structures present on the surface of a *Sarracenia trichome*. They attributed the remarkable water transport speed to the trichome's hierarchical microchannel arrangement. Additionally, they discovered that the optimal mass transfer rate occurs when there are two ribs [16]. Thus, it is evident from the recent literature that using nature-inspired micro/nano-structures can alter the flow performance. In the case of hierarchical structures, as the capillary imbibition is enhanced, however the classical Lucas-Washburn equation (*shown in equation (2)*) cannot predict the flow characteristics.

$$x(t) = \sqrt{\frac{\sigma D_h \cos\theta}{4\mu} t} \tag{2}$$

where, $x(t)$ is the meniscus position varying with time t, D_h is the hydraulic diameter of the channel, and μ is the coefficient of dynamic viscosity of the fluid.

Alternatively, numerical simulations can be utilized to conduct such studies. Numerous research efforts have demonstrated that numerical simulations serve as a valuable preliminary approach, being both cost-effective and time-efficient [17]–[22]. In the present study, numerical simulations have been employed to understand the capillary flow in a hierarchical microchannel, which is in continuation of the previous work published by Kumar et al. [23]. In the previous work, the ribs of the hierarchical channel are perpendicular (*rib angle = 90º*). However, a study conducted by Zhan et al. showed a change in the behavior of water droplet bouncing if the microstructures are inclined at certain angles [24]. Motivated by this consideration, the current study investigates the effects of inclined ribs within hierarchical channels on capillary flow characteristics. The objective of this research is to determine the variation in the imbibition rate of capillary flow when the ribs are not perpendicular, which is a prevalent issue during the fabrication of hierarchical channels.

2. NUMERICAL SIMULATION

2.1 Geometry of microchannel

The schematic of a hierarchical microchannel with a major channel and a minor channel has been designed as shown in Fig. 2. In the present study, the geometry consists of a number of ribs n=2; because it claims to have a high flux ratio in hierarchical channels [16].

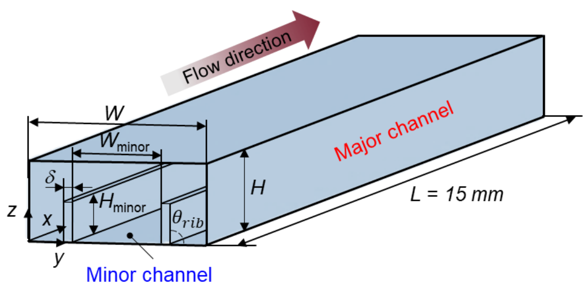

Fig. 2. Geometry of a closed hierarchical microchannel.

The total length of the channel is 15 mm with fixed height (H) and width (W) of the major channel as 100 μm and 200 μm respectively. From the previous work by Kumar et al. [23], it has been established that in the case of the minor channel, the width (W_{minor}), when fixed to be 100 μm, and the height (H_{minor}) to be 10 μm, then yields the highest imbibition rate. The rib thickness δ is 10 μm. The rib angle (θ_{rib}) is changed from 90º to 60º. When the rib angle is 60º, three possible cases have been simulated, as shown in Fig. 3, which have been named / / - type, / \ - type, and \ / - type.

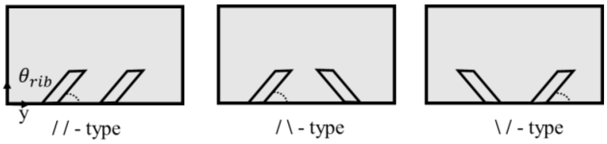

Fig. 3. Simulation cases of rib inclinations.

2.2 Governing Equations

Transient, three-dimensional numerical simulations of capillary flow in a hierarchical microchannel were conducted using the volume-of-fluid (VOF) method. This system includes two incompressible, immiscible fluids: water as the liquid phase and air as the gas phase. The VOF method accounts for surface tension effects [25], [26]. The simulation addresses both the momentum and continuity equations, assuming the flow is laminar, incompressible, Newtonian, and isothermal. The velocity field V is governed by the Navier-Stokes and continuity equations, expressed as follows:

$$\nabla . V = 0 \tag{3}$$

$$\frac{\partial \rho V}{\partial t} + \nabla . (\rho V V) = -\nabla P + \rho g + \nabla . \left(\mu(\nabla V + \nabla^T V)\right) + F_s \tag{4}$$

In Equation (3-4), V denotes the velocity of the fluid mixture, P represents the pressure, t indicates time, and F_s represents the volumetric force due to surface tension at the interface between the fluids. Additionally, ρ and μ stand for the fluid density and dynamic viscosity, respectively. Within this equation, the accumulation and convective momentum terms in each control volume (or cell) ensure a balance among the pressure force, gravitational force, shear force, and the additional force arising from surface tension, F_s. The volumetric force F_s accounts for the effects of surface tension, which is the force that acts on the surface of a liquid due to the attraction between its molecules. In the context of the VOF method, the balance of these forces within each cell of the computational grid is crucial for accurately modeling the capillary-driven flow, capturing the dynamics of how the fluid interface evolves over time.

The physical properties of each fluid are determined by calculating weighted averages based on the volume fraction of the individual fluid present in a single cell. The fluid volume within a cell is computed as $F_{vol} = F.V_{cell}$, where V_{cell} represents the volume of a computational cell and F denotes the liquid volume fraction within that cell. The value of F within a cell should fall between the range of 0 and 1. A value of F = 1 signifies a cell that is filled with liquid, while F = 0 indicates a cell filled with gas. Values of F ranging from 0 to 1 represent the interface between the liquid and gas phases.

To determine the distribution of the liquid volume fraction, an additional passive transport equation is solved, expressed as:

$$\frac{\partial F}{\partial t} + V.\nabla F = 0 \quad (5)$$

where F is the fraction representing the liquid volume relative to the total volume of the control cell. Using this volume fraction function, the physical properties of the mixture are derived computationally as follows:

$$\rho = F\rho_2 + (1 - F)\rho_1 \quad (6)$$

$$\mu = F\mu_2 + (1 - F)\mu_1 \quad (7)$$

Here, ρ and μ are the density and dynamic viscosity, respectively, with subscripts 1 and 2 representing the gas and liquid phases. As capillary forces mainly depend on surface forces, the surface tension is computed using the continuum surface force (CSF) model. The model equation is:

$$F_s = \sigma\kappa\nabla F \quad (8)$$

In the CSF model, the surface tension remains constant across the surface, and forces acting perpendicular to the interface are considered. To calculate the surface curvature, κ, the following equation is used:

$$k = \frac{1}{|n|}\left(\left(\frac{n}{|n|}.\nabla\right)|n| - \nabla.|n|\right) \quad (9)$$

Here, $\mathbf{n} = \nabla F$ denotes the normal vector. The contact angle θ includes wall adhesion forces, represented by:

$$\hat{n} = \hat{n}_w + \hat{t}_w \, sin \, sin \, \theta \quad (10)$$

To find the liquid volume fraction and velocity field solution in this study, equations (3) to (10) are solved iteratively, considering appropriate initial and boundary conditions. Gravity's influence is not considered in this study since the Bond number (Bo = $\rho gH^2/\sigma$) is significantly lower than unity.

2.3 Initialization & boundary conditions

At the initial time t=0, the liquid meniscus is positioned 1 mm from the inlet of the hierarchical channel. The channel walls are subjected to a no-slip boundary condition, meaning the fluid at the wall has zero velocity relative to the wall. The surface affinity of the walls is determined by the contact angle, which is set at 30 degrees for all walls of both the major and minor channels. A liquid volume fraction of 1 is specified at the inlet, indicating that the entire inlet region is filled with liquid. Conversely, a liquid volume fraction of 0 is assigned at the outlet, indicating the absence of liquid at that location.

In the initial scenario, the rib angle is 90 degrees. For the second scenario, where the rib angle is set at 60 degrees, three different inclinations are defined to assess the effect of rib inclination on the flow characteristics.

2.4 Solution method

In this study, computational fluid dynamics (CFD) simulations were conducted using OpenFOAM *v2012*, a C++ library-based software widely recognized for its application in simulating fluid flow and heat transfer phenomena across various engineering and scientific domains [21], [23], [27], [28]. The simulations utilized a finite volume approach to solve partial differential equations on a 3D unstructured mesh composed of polyhedral cells. To accurately model the sharp interfaces between fluids in capillary-driven flow, the solver employed the Volume of Fluid (VOF) two-phase algorithm. Given the transient nature of the problem, selecting an appropriate time step was critical to ensure numerical stability. A Courant-Friedrichs-Lewy (CFL) number of 0.1 was targeted to maintain stability, allowing the interface to cross 10% of a grid cell's width during each time step in the VOF computation. To integrate pressure and velocity fields and perform pressure correction, the solver employed the Pressure Implicit with Splitting of Operators (PISO) algorithm. Additionally, an artificial compression term was introduced into the VOF equation to compress the interface and prevent separation, particularly in diverging flows. These methods and algorithms collectively ensured the accuracy and stability of the numerical simulations, facilitating detailed analysis of complex capillary-driven flows and the precise capture of intricate fluid interfaces. Some important parameters used in the simulations were surface tension, σ = 0.0707 N/m, Courant $Number_{maximum}$ = 0.2, and *Gauss linear* scheme with time step Δt = 1e-5 s. The structured hexahedral mesh consisted of ~580,000 cells as shown in Fig. 4. Hexahedral cells align better with the flow direction, reducing numerical diffusion and precisely capturing sharp fluid interfaces. This structured mesh allows for higher resolution of interfaces and improves computational efficiency by reducing the cell count compared to unstructured meshes. Moreover, the structured nature of hexahedral meshes enhances numerical stability, essential for accurately solving the Navier-Stokes equations and maintaining interface integrity in VOF simulations, leading to more reliable and efficient results.

Fig. 4. Structured hexahedral mesh.

To ensure the accuracy and reliability of the numerical simulations, a comprehensive analysis was conducted to verify the independence of the results for both time step and mesh size. Despite OpenFOAM's adaptive time stepping, simulations were performed for time step independence with various fixed time steps. The results were compared and found to be consistent, indicating that the solutions were not significantly affected by the time step size. A mesh refinement study was carried out to determine mesh independence. Simulations were conducted with increasing mesh resolutions until further refinement, beyond 580,000 cells, resulted in negligible changes in the key simulation outputs. This confirmed that the chosen mesh resolution was sufficient to capture the necessary details without compromising the accuracy of the results. The simulations were executed within a high-performance computing (HPC) environment, utilizing a clustered parallel setup facilitated by the open message passing interface (OpenMPI) library. The computational mesh was decomposed using the *decomposePar* utility, which partitioned the computational domain across 150 processors, distributed over 2 nodes. This parallel processing approach significantly enhances computational efficiency and reduces the time required for simulations, allowing for the handling of complex and large-scale fluid dynamics problems with greater precision and speed.

3. RESULTS AND DISCUSSION

3.1 Validation

Before proceeding with simulations for the present study, a basic model consisting of a closed rectangular microchannel with no hierarchical structure has been validated against the current theory which is the L-W equation (*shown in equation (2)*). The simulated channel has a total length of 30 mm, with a height (H) of 100 μm and a width (W) of 200 μm. The contact angle for all four channel walls is uniformly set at 80 degrees. The simulation results were compared with the established theory of capillary flow described by the Lucas-Washburn (L-W) equation for closed channels. Figure 5 demonstrates a strong agreement between the theoretical predictions and the numerical simulation results.

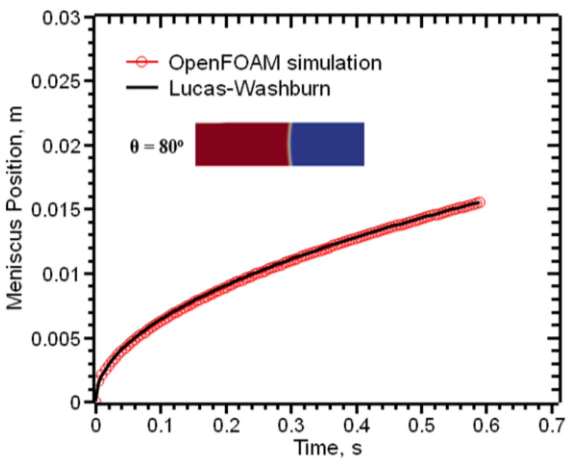

Fig. 5. Comparison of Lucas-Washburn theory and numerical simulation results.

3.2 Capillary performance in hierarchical channel with rib angle = 90 degrees

The previous study conducted by Kumar et al. showed that when the width of minor channel W_{minor} is fixed at 100 μm then the maximum imbibition was observed when minor channel height H_{minor} = 10 μm [23].

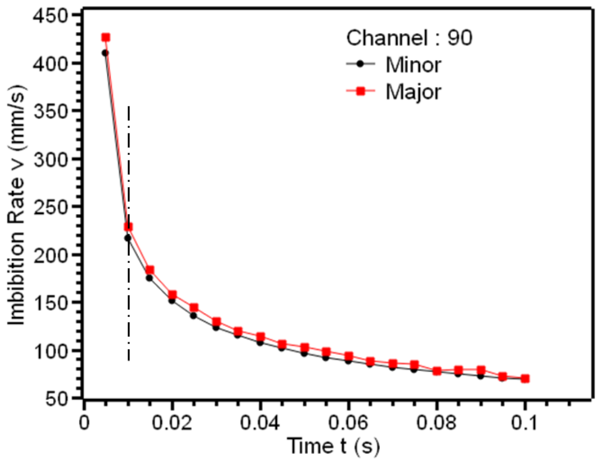

Fig. 6. Change in imbibition rate in major and minor channels of the hierarchical channel when the rib angle = 90°.

Figure 6 illustrates the imbibition rate of capillary flow in a hierarchical channel with a rib angle of 90 degrees, meaning the ribs are perpendicular to the bottom surface or wall of the channel. A noticeable difference in the imbibition rates between the major and minor channels is observed. This discrepancy is primarily attributed to the corner flow occurring in the major channels, which enhances the overall imbibition rate as the fluid (*water*) tends to move more rapidly along the corners due to the combined effects of surface tension and the geometric confinement of the channel. The mean imbibition rate at *t*=0.1 sec is 127.34 mm/s and 121.04 mm/s for the major and minor channels respectively.

3.3 Capillary performance in hierarchical channel with rib angle = 60 degrees

There is a notable variation in imbibition rates in hierarchical channels when the ribs are not perpendicular to the bottom wall or surface. During the fabrication process or repeated experiments, rib inclination can occur. In the present study, the ribs are inclined at 60 degrees, with three possible configurations. Figure 7 illustrates the change in imbibition rate of capillary flow in a hierarchical channel with a rib angle of 60 degrees, showing an inclination of the / / - type.

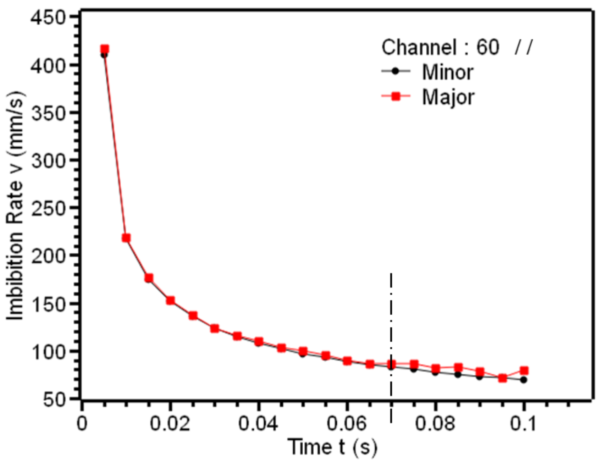

Fig. 7. Change in imbibition rate in major and minor channels of the hierarchical channel when the rib angle = 60° / / - type.

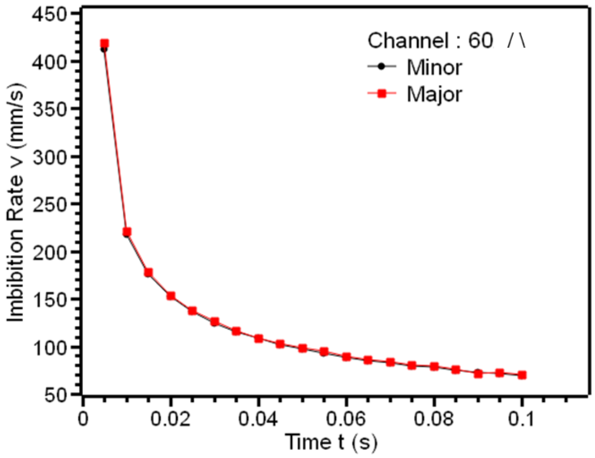

Fig. 8. Change in imbibition rate in major and minor channels of the hierarchical channel when the rib angle = 60° / \ - type.

In the case of the 60° / / - type channel, the imbibition rate in the major and minor channels is almost equal until *t*=0.07 seconds. Once the corner flow kicks in, the change in imbibition rates in major and minor channels begins which is evident from Fig. 7. The mean imbibition rate at *t*=0.1 sec is 124.40 mm/s and 121.53 mm/s for the major and minor channels respectively. On the other hand, for 60° / \ - type channel, there is no difference in the imbibition rate in major and minor channels shown in Fig. 8. The mean imbibition rate for 60° / \ - type at *t*=0.1 sec is 123.25 mm/s and 121.78 mm/s for the major and minor channels respectively. At last, in the case of the 60° \ / - type channel, there is a slight change in imbibition between major and minor channels after *t*=0.095 seconds. The effect of corner flow is almost negligible. The mean imbibition rate at *t*=0.1 sec is 122.70 mm/s and 121.06 mm/s for the major and minor channels respectively.

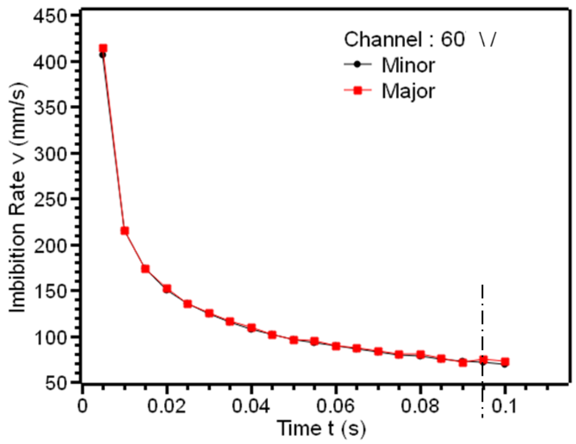

Fig. 9. Change in imbibition rate in major and minor channels of the hierarchical channel when the rib angle = 60° \ / - type.

3.4 Comparison of capillary performance

In this section, a comprehensive comparison of the imbibition rates in all four types of hierarchical channels studied in this paper has been presented.

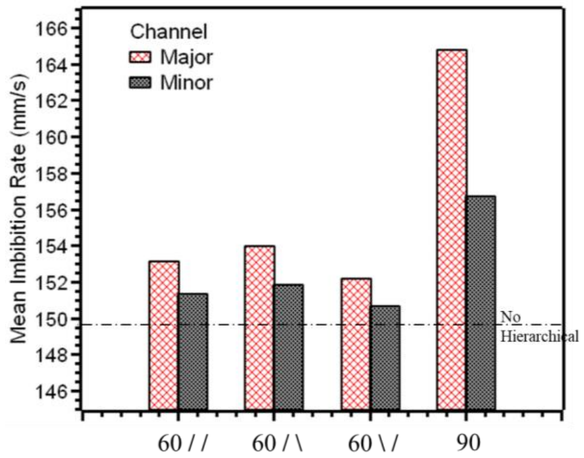

Fig. 10. Difference in the mean imbibition rates for major and minor channels for the given types.

It can be observed from Fig. 10 that, in channels with perpendicular ribs i.e. when rib angle=90°, the major channels show enhanced imbibition rates due to corner flow, which increases the overall wetted surface area. Conversely, in channels with inclined ribs i.e. when rib angle=60°, a reduction in imbibition rates is observed, which is likely due to decreased effective capillary action and altered flow dynamics. However, in any case, the capillary performance in the hierarchical channel is still better than a microchannel with no hierarchical structure.

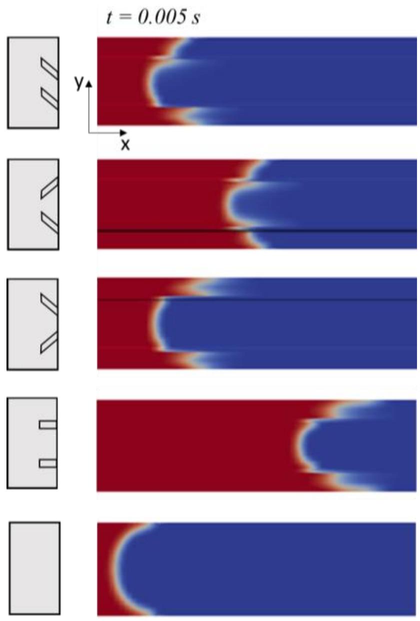

Fig. 11. Meniscus space for given types.

The shape of the meniscus in a hierarchical channel can significantly enhance fluid flow, influenced by whether the ribs are perpendicular or inclined. It can be seen from Fig. 11. that, when the ribs are perpendicular to the channel wall i.e. the rib angle = 90°, the meniscus typically forms a sharp, well-defined shape at the interface between the liquid and air. This configuration maximizes the capillary pressure, driving the liquid more effectively through the channel. The perpendicular orientation of the ribs aids in maintaining a consistent and stable flow, as the meniscus conforms closely to the ribbed structure, promoting efficient fluid movement. However, channels with inclined ribs (i.e. the rib angle = 60°) can create variations in capillary pressure along the flow path, potentially creating a barrier for the fluid movement within the channel.

4. CONCLUSION

In this study, we conducted three-dimensional numerical simulations of capillary-driven flow in closed hierarchical microchannels to investigate the impact of rib angles on capillary performance. The simulations were performed using the OpenFOAM-based Volume of Fluid (VOF) method, examining rib angles of 90° and 60° with variations in inclination types. The results demonstrated that rib inclinations significantly hinder capillary flow performance, reducing the imbibition rate considerably. While different inclination types within the same rib angle showed minimal differences, it is clear that any inclination disrupts corner flow, thereby diminishing capillary performance. This research underscores the critical importance of precise rib fabrication in hierarchical channels for optimizing capillary action. Understanding these effects can guide future designs and improve the efficiency of fluid transport in microchannel applications.

ACKNOWLEDGMENTS

This work was supported by the Ministry of Education, Science and Culture of the Japanese Government through the Grant-in-Aid for Scientific Research, Project No. 22K18773 & 22H01416, the research supercomputing services by Kyushu University, and Osaka University.

5. REFERENCES

[1] E. Berthier, A. M. Dostie, U. N. Lee, J. Berthier, and A. B. Theberge, "Open Microfluidic Capillary Systems," *Analytical Chemistry*, vol. 91, no. 14. American Chemical Society, pp. 8739–8750, 01-Jul-2019.

[2] L. Xue, C. Guo, Y. Zhang, Y. Xu, and B. Li, "Parametrical Study on the Capillary Flowing Characteristics of the Parallel Microchannel Array," *Crystals*, vol. 12, no. 7, Jul. 2022.

[3] J. Bao and G. Nagayama, "Optimization for ultrafast capillary-driven flow in open rectangular microchannels," *International Journal of Heat and Mass Transfer*, vol. 201, Feb. 2023.

[4] É. Ruiz-Gutiérrez *et al.*, "The long cross-over dynamics of capillary imbibition," *Journal of Fluid Mechanics*, vol. 939, May 2022.

[5] C. Trejo-Soto, E. Costa-Miracle, I. Rodriguez-Villarreal, J. Cid, T. Alarcón, and A. Hernández-Machado, "Capillary filling at the microscale: Control of fluid front using geometry," *PLoS ONE*, vol. 11, no. 4, Apr. 2016.

[6] J. Cai, Y. Chen, Y. Liu, S. Li, and C. Sun, "Capillary imbibition and flow of wetting liquid in irregular capillaries: A 100-year review," *Advances in Colloid and Interface Science*, vol. 304. Elsevier B.V., 01-Jun-2022.

[7] H. Chen *et al.*, "Surface Tension Transport of," *Analytical Chemistry*, vol. 10, no. 2, pp. 1–20, Oct. 2024.

[8] Z. Wang *et al.*, "Three-Dimensional Open Water Microchannel Transpiration Mimetics," *ACS Applied Materials and Interfaces*, vol. 14, no. 26, pp. 30435–30442, 2022.

[9] D. Jafari, W. W. Wits, and B. J. Geurts, "Metal 3D-printed wick structures for heat pipe application: Capillary performance analysis," *Applied Thermal Engineering*, vol. 143, no. July, pp. 403–414, 2018.

[10] Y. Zhang, Y. Gan, L. Zhang, D. Zhang, and H. Chen, "Surface-tension-confined channel with biomimetic microstructures for unidirectional liquid spreading," *Micromachines*, vol. 11, no. 11, pp. 1–14, 2020.

[11] X. Pu, G. J. Li, and Y. H. Liu, "Progress and perspective of studies on biomimetic shark skin drag reduction," *ChemBioEng Reviews*, vol. 3, no. 1, pp. 26–40, 2016.

[12] H. Li *et al.*, "Effects of inclination angle and heat power on heat transfer behavior of flat heat pipe with bionic grading microchannels," *Applied Thermal Engineering*, vol. 206, no. May 2021, p. 118079, 2022.

[13] P. Comanns *et al.*, "Directional, passive liquid transport: The Texas horned lizard as a model for a biomimetic 'liquid diode,'" *Journal of the Royal Society Interface*, vol. 12, no. 109, 2015.

[14] J. Ju, H. Bai, Y. Zheng, T. Zhao, R. Fang, and L. Jiang, "A multi-structural and multi-functional integrated fog collection system in cactus," *Nature Communications*, vol. 3, pp. 1–6, 2012.

[15] T. Wu *et al.*, "Bio-inspired hierarchical wearable patch for fast sweat collection," *Biosensors and Bioelectronics*, vol. 260, no. March, p. 116430, 2024.

[16] H. Chen *et al.*, "Ultrafast water harvesting and transport in hierarchical microchannels," *Nature Materials*, vol. 17, no. 10, pp. 935–942, Oct. 2018.

[17] L. Yang, A. Ładosz, and K. F. Jensen, "Analysis and simulation of multiphase hydrodynamics in capillary microseparators," *Lab on a Chip*, vol. 19, no. 4, pp. 706–715, 2019.

[18] J. Ko, N. Takata, K. Thu, and T. Miyazaki, "Dynamic Simulation of a Thermal Management System Consisting of a CO_2 Heat Pump and a Water-Loop," pp. 39–43, 2019.

[19] A. A. Saha, S. K. Mitra, M. Tweedie, S. Roy, and J. McLaughlin, "Experimental and numerical investigation of capillary flow in SU8 and PDMS microchannels with integrated pillars," *Microfluidics and Nanofluidics*, vol. 7, no. 4, pp. 451–465, 2009.

[20] A. Bamshad *et al.*, "Capillary Flows : Dynamics & Geometry Effects," *5th RSI International Conference on Robotics and Mechatronics, IcRoM 2017*, no. IcRoM, pp. 432–438, 2017.

[21] D. Gründing *et al.*, "Capillary Rise -- A Computational Benchmark for Wetting Processes," Jul. 2019.

[22] T. T. Zhang *et al.*, "Numerical study on flow rate limitation of open capillary channel flow through a wedge," *Advances in Mechanical Engineering*, vol. 8, no. 4, pp. 1–11, Apr. 2016.

[23] G. Kumar, D. Zhang, and G. Nagayama, "OpenFOAM-based Numerical Simulation on Capillary Flow in Closed Hierarchical Microchannels," *International Exchange and Innovation Conference on Engineering and Sciences*, vol. 9, pp. 343–348, 2023.

[24] Z. Zhan, Z. Wang, M. Xie, Y. Chen, and H. Duan, "Programmable Droplet Bouncing on Bionic Functional Surfaces for Continuous Electricity Generation," *Advanced Functional Materials*, vol. 34, no. 1, pp. 1–9, 2024.

[25] B. a. Nichita, I. Zun, and J. R. Thome, “A VOF method coupled with a dynamic contact angle model for simulation of two-phase flows with partial wetting,” *7th International Conference on Multiphase Flow*, pp. 1–8, 2010.
[26] A. Ashish Saha and S. K. Mitra, “Effect of dynamic contact angle in a volume of fluid (VOF) model for a microfluidic capillary flow,” *Journal of Colloid and Interface Science*, vol. 339, no. 2, pp. 461–480, Nov. 2009.
[27] K. J. Vachaparambil and K. E. Einarsrud, “Comparison of surface tension models for the volume of fluid method,” *Processes*, vol. 7, no. 8, 2019.
[28] D. A. Hoang, V. Van Steijn, L. M. Portela, M. T. Kreutzer, and C. R. Kleijn, “Modeling of low-capillary number segmented flows in microchannels using OpenFOAM,” in *AIP Conference Proceedings*, 2012, vol. 1479, no. 1, pp. 86–89.